arXiv:1805.12285v2 [astro-ph.SR] 20 May 2019

The Multi-Instrument (EVE-*RHESSI*) DEM for Solar Flares, and Implications for Non-Thermal Emission

JAMES M. MCTIERNAN,[1] AMIR CASPI,[2] AND HARRY P. WARREN[3]

[1]*Space Sciences Laboratory, University of California, Berkeley, CA 94720*
[2]*Southwest Research Institute, Boulder, CO 80302*
[3]*Space Science Division, Naval Research Laboratory, Washington, DC 20375*

ABSTRACT

Solar flare X-ray spectra are typically dominated by thermal bremsstrahlung emission in the soft X-ray ($\lesssim$10 keV) energy range; for hard X-ray energies ($\gtrsim$30 keV), emission is typically non-thermal from beams of electrons. The low-energy extent of non-thermal emission has only been loosely quantified. It has been difficult to obtain a lower limit for a possible non-thermal cutoff energy due to the significantly dominant thermal emission.

Here we use solar flare data from the EUV Variability Experiment (EVE) on-board the *Solar Dynamics Observatory* (*SDO*) and X-ray data from the *Reuven Ramaty High Energy Spectroscopic Imager* (*RHESSI*) to calculate the Differential Emission Measure (DEM). This improvement over the isothermal approximation and any single-instrument DEM helps to resolve ambiguities in the range where thermal and non-thermal emission overlap, and to provide constraints on the low-energy cutoff.

In the model, thermal emission is from a DEM that is parametrized as multiple gaussians in $Log(T)$. Non-thermal emission results from a photon spectrum obtained using a thick-target emission model. Spectra for both instruments are fit simultaneously in a self-consistent manner.

Our results have been obtained using a sample of 52 large (*GOES* X- and M-class) solar flares observed between February 2011 and February 2013. It turns out that it is often possible to determine low-energy cutoffs early (in the first two minutes) during large flares. Cutoff energies at these times are typically low, less than 10 keV, when assuming coronal abundances. With photospheric abundances, cutoff energies are typically ~10 keV higher, in the ~17–25 keV range.

*Keywords:* Sun: corona — Sun: flares — Sun: UV radiation — Sun: X-rays, gamma rays

1. INTRODUCTION

Solar flare X-ray emission is commonly characterized as either "thermal" or "non-thermal" (Fletcher et al. 2011). In the standard flare model (e.g., Shibata 1996) the thermal component is "soft" X-ray emission due to bremsstrahlung radiation from a heated plasma, and the non-thermal component is "hard" X-ray emission due to bremsstrahlung from a beam of particles (usually assumed to be electrons) accelerated in a reconnection-related process in the solar corona. (See, for example, the review by Benz 2017).

The relative magnitudes and timing of the hard and soft components are illustrated in Figure 1, which shows X-ray emission observed by the *Reuven Ramaty High Energy Solar Spectroscopic Imager* (*RHESSI*; Lin et al. 2002) and by the

Corresponding author: James M. McTiernan
jimm@ssl.berkeley.edu

Geostationary Operational Environmental Satellite (*GOES*; Donnelly et al. 1977) X-ray Sensor from a solar flare that occurred on 2011 February 15. The *RHESSI* light curves in the energy bands of 6–12 keV, 12–25 keV, 25–50 keV, and 50–100 keV show typical behavior; the lowest energy (thermal "soft" X-ray) emission is gradual, the highest energy (non-thermal "hard" X-ray) emission is impulsive, and the intermediate-energy emission shows both characteristics. Flares typically exhibit the "Neupert Effect," in which the derivative of the gradual soft X-ray time profile is similar to the time profile of impulsive hard X-rays (Neupert 1968).

Since the thermal and non-thermal emissions overlap in energy, it has been a difficult problem to find a low-energy limit for the electrons responsible for the non-thermal emission, with estimates ranging from as low as 5–6 keV (Kane et al. 1992) to values as high as 50 keV or more (Sui et al. 2007; Warmuth et al. 2009) and many values in between (Aschwanden et al. 2016). This value is important for determination of the energy released in non-thermal elec-
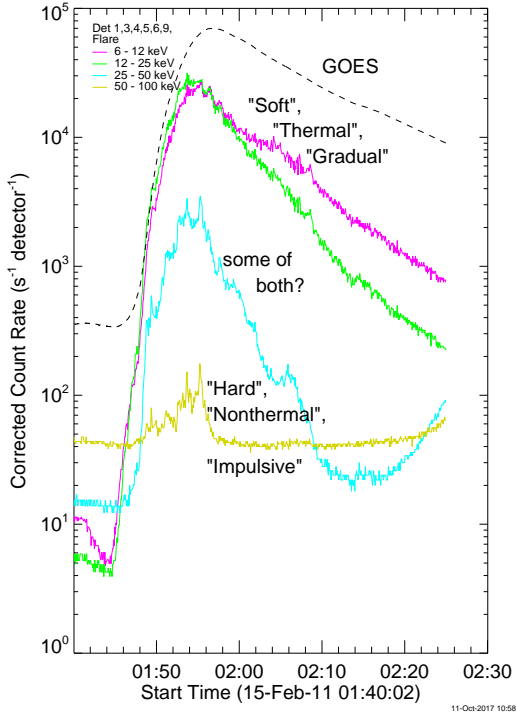
Figure 1. *RHESSI* and *GOES* light curves for an X-class flare on 2011 February 15. *RHESSI* curves (colors) are for the energy ranges of 6–12, 12–25, 25–50, and 50–100 keV. The *GOES* curve (dashed) is for the long wavelength (nominally 1–8 Å) channel.

trons; a difference of just 10 keV in this parameter can result in orders of magnitude changes in the total energy required for the flare.

In this work, we combine *RHESSI* X-ray data with extreme ultraviolet (EUV) data from the *EUV Variability Experiment* (EVE; Woods et al. 2012) instrument on-board the *Solar Dynamics Observatory* (*SDO*; Pesnell et al. 2012) to calculate the Differential Emission Measure (DEM) for the thermal component of solar flares. This improvement over the isothermal approximation, and over DEMs derived from *RHESSI* alone, helps to resolve the ambiguity in the energy range where the thermal and non-thermal components may have similar photon fluxes, and hence where it is often difficult to differentiate between them using more naïve methods.

Previously we have shown that even though *RHESSI* and EVE are very different instruments, they can still be used in combination to self-consistently obtain the DEM in the ~2–50 MK range (Caspi et al. 2014b). Because of the simultaneously complementary and overlapping temperature sensitivities of the two instruments, their joint DEM converges more stably, is more robust, and is significantly more accurate—particularly at the extreme ends of the temperature range—than when using one instrument in isolation. In that prior work, although we did fit the non-thermal component of the *RHESSI* spectra, we did not consider the resulting

non-thermal parameters in any detail. In this work we are interested in constraining low-energy cutoffs in the "residual" non-thermal spectrum, i.e., the *RHESSI* spectrum that is left over after the DEM has accounted for the bulk of the soft X-ray emission. Ideally, we would calculate the DEM using EVE alone, to independently determine the thermal X-ray emission which we would then subtract from *RHESSI* to obtain the residual, presumably entirely non-thermal, spectrum. However, this is not possible since the EVE DEM is not well-constrained at high ($\gtrsim$20 MK) temperature (Warren et al. 2013) and the resulting predicted thermal X-ray component can therefore be inaccurate (Caspi et al. 2014b), sometimes quite significantly. So, as in the prior work, we will fit the DEM plus non-thermal spectra simultaneously, with EVE and *RHESSI* together. We then use χ^2 values to determine limits for the low-energy cutoff in the non-thermal emission.

In the following section we discuss the DEM plus non-thermal model for the emission. This is followed by a description of the data set, then the results of the calculation, followed by discussion of the results.

2. DEM PLUS NON-THERMAL MODEL

The method we use for calculating the DEM has been presented in detail in Warren et al. (2013) and Caspi et al. (2014b); here we only give a brief overview. In the fitting model, the DEM is parametrized by a set of 11 Gaussian functions of $Log(T)$, equally spaced in the range of $Log(T)$ from 6.2 (~1.6 MK) to 7.8 (~63 MK). The width of each Gaussian is $dLog(T) = 0.02$, and is held fixed in the model. Only the Gaussian amplitudes vary. The amplitude of the 11th Gaussian (at ~63 MK) is held fixed to a small value, to increase the stability of the calculation, so the model DEM is effectively set to be zero at $\gtrsim$60 MK. The original calculation (Caspi et al. 2014b) used 10 Gaussians and did not limit the amplitude for the highest temperature component; the limit on the additional Gaussian imposed here improves fitting stability and is consistent with prior studies that found that flare plasma temperatures do not exceed $\gtrsim$50 MK even for the largest recorded solar flares (Caspi et al. 2014a; Warmuth & Mann 2016). Following our previous work, we use coronal abundances for the demonstration of the DEM calculation, but we have also done the calculations assuming photospheric abundances and will discuss the effects of abundance variation, particularly for Fe.

The next step is to use the CHIANTI IDL package (Dere et al. 1997; Landi et al. 2013) to calculate the thermal EUV spectral irradiance from the model DEM, for comparison with the EVE data. For *RHESSI*, the X-ray photon flux is calculated using `chianti_kev`, a database of pretabulated (for speed) CHIANTI-generated X-ray spectra, from the IDL SolarSoft (SSW; Freeland & Handy 1998) `xray` package, integrated over the instrument response to recover a

model *RHESSI* spectrum[1]. Note that the original model discussed by Caspi et al. (2014b) separately fit the Fe and Fe-Ni line complexes (at ∼6.7 and ∼8 keV). Here we use the line emission as calculated directly by the CHIANTI package.
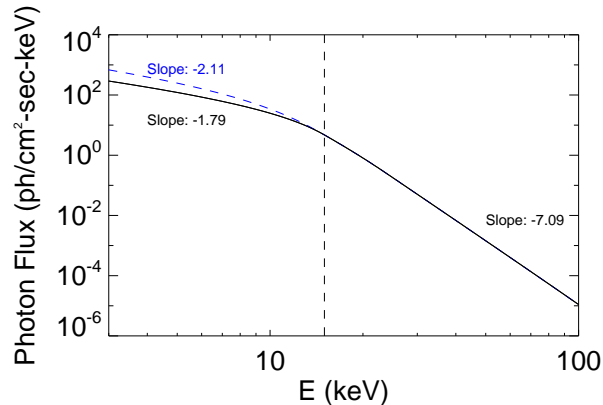
Figure 2. A sample thick-target X-ray photon spectrum, for $E_c = 15$ keV (dashed vertical line) and input electron spectral power-law index $\delta = -7.8$. Note that a sharp cutoff at E_c in the electron energy spectrum translates to a gradual rollover in the photon spectrum at energies below E_c. The blue dashed line below 10 keV shows the photon spectrum for a model with flat electron spectrum below E_c, see Section 6 for discussion.

To completely fit the *RHESSI* spectrum, a non-thermal emission model is necessary in addition to the thermal (DEM) component. We use the thick-target model (Brown 1971), as implemented by f_thick2 in the SSW xray package. In this model, the non-thermal emission is assumed to be due to bremsstrahlung radiation from a beam of electrons, excited in the corona by an undetermined process, impacting the chromosphere and depositing all of their energy there. Although the electrons are beamed along magnetic field lines, the distribution of pitch angles (defined as the angle between the electron velocity vector and the local magnetic field) is assumed to be isotropic. This is a reasonable assumption for the relatively low electron energies in which we are interested (Leach & Petrosian 1981; McTiernan & Petrosian 1990). f_thick2 uses the Haug (1997) approximation to the relativistic Bethe-Heitler bremsstrahlung cross-section (Eq. 3BN of Koch & Motz 1959). For an initial power-law electron beam with spectral index (negative log-log slope) δ and a low-energy cutoff at electron energy E_c, we expect to see a break (or, more correctly, a rollover) in the photon spectrum slightly below the electron cutoff energy, with the spectrum below E_c being flatter than the spectrum above, as shown in Figure 2. The photon spectral index below the cutoff has an asymptotic value of ∼1.8,

which is independent of the value above the cutoff. In Figure 2 the photon index γ above the cutoff is ∼7.1 (for input electron $\delta = 7.8$).

In our model, using f_thick2, the electron distribution is parametrized as a broken power law, with both low- and high-energy cutoffs. The non-thermal parameters are: A_0, the total integrated electron flux, in units of 10^{35} electrons s^{-1}; A_1, the power-law index of the electron distribution function below a break energy E_{br}; A_2, the break energy E_{br}, in keV; A_3, the power-law index above E_{br}; A_4, the low-energy cutoff E_c, in keV; and A_5, the high-energy cutoff, in keV. Including the 11 parameters for the DEM and these 6 for the non-thermal model, there are 17 total model parameters.

The spectral fit procedure minimizes $\chi^2 = \chi^2_{RHESSI} + \chi^2_{EVE}$, which for each instrument is defined as

$$\chi^2 = \sum_i (f_{i,model} - f_{i,obs})^2 / \sigma_i^2 \quad, \qquad (1)$$

where $f_{i,model}$ is the model data (spectral irradiance for EVE, photon count rate for *RHESSI*), $f_{i,obs}$ is the observed data, and σ_i is the measurement uncertainty. For *RHESSI*, the uncertainty in each energy channel is estimated using Poisson statistics: $\sigma_{i,RHESSI} = \sqrt{f_{i,obs}/\delta t}$, where δt is the time interval duration. For EVE, the uncertainty is given by the observed standard deviation (from calibrated Level 2 EVE data; Hock et al. 2012) of the individual irradiance measurements during the time interval, divided by the square root of the number of 10 s spectra averaged for the time interval (Warren et al. 2013).

For EVE, a pre-flare background spectrum is subtracted to isolate the flare emission; this is obtained for a three-minute interval immediately before the associated *GOES* flare start time. For *RHESSI* the process is more complicated, because the background level depends on spacecraft position; it increases at high geomagnetic latitude. The background levels shown in McTiernan (2009b), valid for the 2002–2006 period, have the appropriate latitude variation but are not applicable for the time intervals used here due to long-term detector changes that result in higher overall background levels later in the mission. Here, for a given flare, we use the background spectrum during the nearest low-latitude spacecraft night interval, accounting for the long-term increase in background values. The spectrum is further modified for latitude variations using the results presented by McTiernan (2009b).

Figure 3 is a diagnostic plot that we use to check the goodness of fit for the full process. The upper left corner shows the (recovered) model DEM. The upper right shows a comparison plot of the *RHESSI* count spectrum, with black denoting the observed data and red the data expected from the model. Just below we show a plot of the residuals for the *RHESSI* portion of the fit (normalized by the uncertainty in each energy channel). The lower panel shows a comparison of the

---

[1] See https://hesperia.gsfc.nasa.gov/rhessidatacenter/software/installation.html
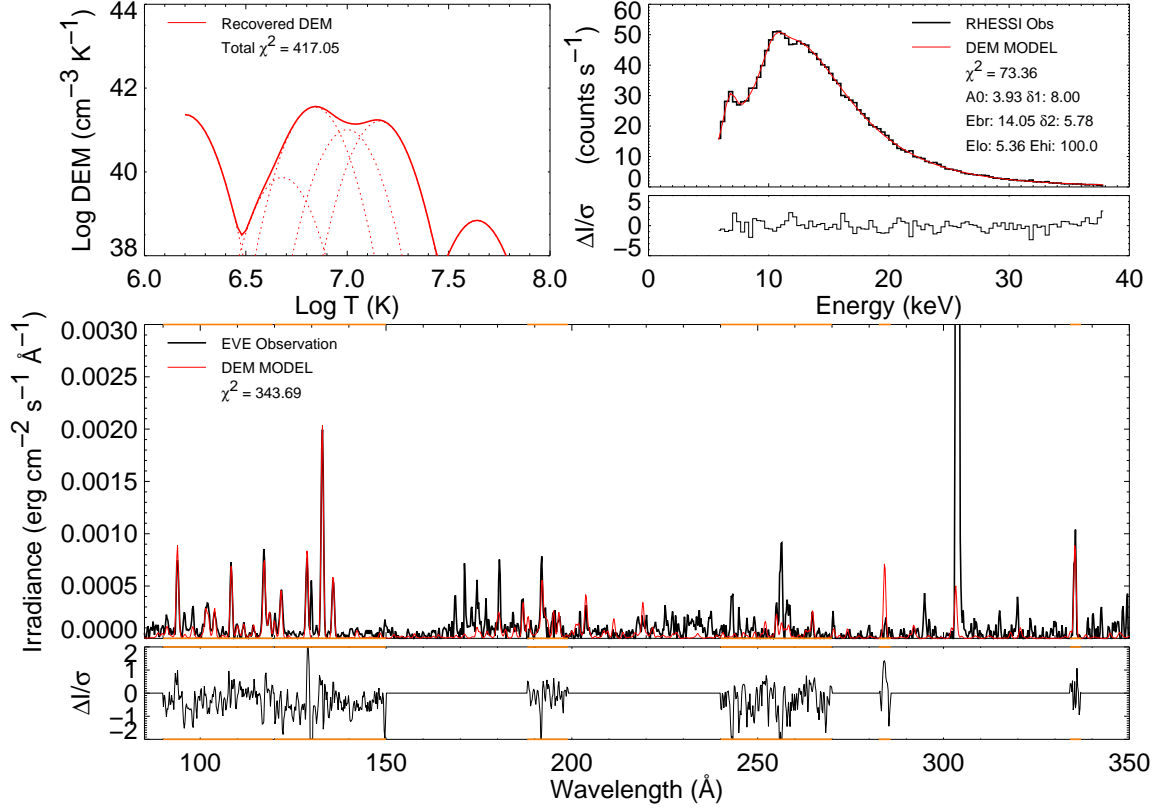
Figure 3. Diagnostic plot showing the goodness of fit early in the M7 flare of 2011 February 13 at 17:32:36 UT. Upper left: Log(DEM). Upper right: *RHESSI* count rate spectrum and residuals. Lower: EVE spectrum and residuals. Orange wavelength ranges in the EVE plots include prominent flare lines and are used for fitting; non-orange ranges are ignored.

EVE spectrum, with observed data in black, and model data in red. Note that not all of the EVE spectrum is used for fitting; we only consider wavelength bands that include prominent spectral lines associated with flares (these are, mostly, relatively high-temperature Fe lines; see Warren et al. 2013 for more details), highlighted in orange. The residual values for the EVE spectrum are shown in the bottom-most panel.

There are many more data points used in each EVE spectrum (400) than there are in the typical *RHESSI* spectrum (100), so we change the weighting of the EVE data in the joint fits by scaling the EVE uncertainties by a constant factor. The actual weight is calculated by finding the minimum value of $\sigma_{i,EVE}/f_{i,EVE}$ and re-scaling so that this value is equal to 0.04, that is, the uncertainty is always at least 4% of the observed data value. This is done to ensure that *RHESSI* data points are sufficiently considered during the fit process; Figure 4 shows a comparison of spectra for the limited (weighted) versus unlimited fit. As is shown in the bottom panel, without these limits to the EVE uncertainties, the *RHESSI* spectrum is not fit well in the full process, particularly in the 6–7 keV range. Typically, the scaling factor is between 1 and 5; for the example shown here the factor is 2.42.

More information regarding the inter-calibration of EVE and *RHESSI* and comparisons with *GOES* XRS data, not shown in (Caspi et al. 2014b), can be found in the appendix.

3. DATA SET

From Figure 1, we can see that the relative amount of thermal to non-thermal emission increases over time during an event. When the non-thermal component is only a small a fraction of the total emission, it becomes difficult to constrain the low-energy cutoff E_c through spectral fitting. Thus, we would like to perform this calculation as early during a flare as possible.

Figure 5 shows a *RHESSI* spectrum early during a flare when the thermal component is not overwhelmingly large. As a first cut, for demonstrative purpose, the spectrum has been fit using two isothermal components (red, blue) and a non-thermal component (green). Even in the ≲10 keV range, the photon flux from the non-thermal component is not much smaller than that for thermal emission; this makes this time interval a good candidate for possibly isolating a cutoff energy. Conversely, Figure 6 shows a spectrum for a later time interval when the thermal component is much more prominent. Here, the "crossover" energy, where the thermal and non-thermal emissions are approximately the same, is ∼30 keV. Below this crossover energy, the non-thermal
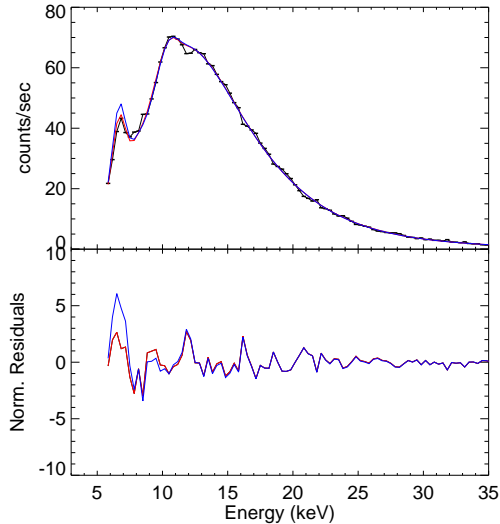
Figure 4. Comparison of *RHESSI* spectral fits for the same time range as Figure 3 (2011 February 13, 17:32:36 UT). Top: black horizontal lines – observed count rate spectrum; red line – model results for "weighted" fit (i.e., where EVE uncertainties are increased so *RHESSI* data more strongly influences the fit process); blue line – model results for "unweighted" fit. Bottom: normalized fit residuals for both cases; the unweighted model clearly yields a poorer fit to the *RHESSI* data at lower energies (where thermal emission dominates).
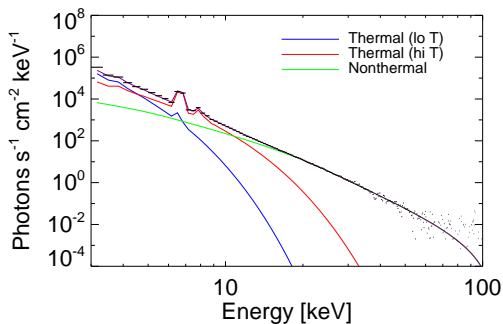
Figure 5. *RHESSI* photon spectrum for 2011 February 13, 17:32:36 UT, fit with two isothermal components (red, blue) and a non-thermal component (green). Early in the flare, the ratio of non-thermal to thermal emission is high, making it easier to estimate the low-energy cutoff of the non-thermal electron distribution.

contribution to the total model becomes vanishingly small (<1% for energies $\lesssim$15 keV), and it is clear that a spectral rollover corresponding to an electron cutoff E_c can "hide" nearly anywhere under the dominant thermal emission below the crossover energy. Thus, E_c would be constrained only as a relatively high upper limit, and this kind of spectrum is not a good candidate for finding E_c. For this reason, we restrict our analysis to the first two minutes of the flares in our sample.
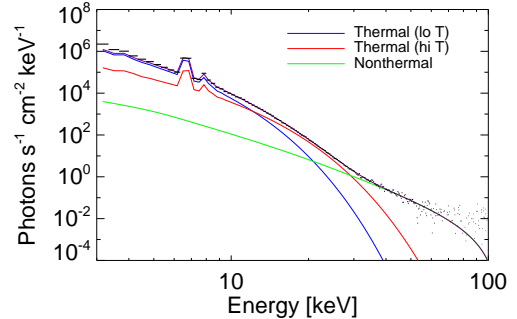

Figure 6. *RHESSI* spectrum for 2011 February 13, 17:35:08 UT, again fit with two isothermal components (red, blue) and a non-thermal component (green). At later times in an event, the thermal emission dominates over the non-thermal at lower energies, making the low-energy cutoff difficult to estimate except as an upper limit.

For this study, we work with a sample of 52 flares observed by both EVE and *RHESSI* during the period from February 2011 to February 2013. Each flare is of *GOES* class M or larger and has X-ray emission observed by *RHESSI* at energies above 50 keV. From each flare, we isolated one or two time intervals of approximately one minute duration with good conditions, i.e., occurring during the first two minutes of the "impulsive" emission >25 keV, with a discernible non-thermal component, with a relatively flat high-energy spectrum (thick-target electron spectral index $\delta < 9$), and with a good signal-to-noise ratio up to at least 50 keV. From these 52 flares, we found 61 appropriate time intervals in 38 flares for which we found good results (reduced $\chi^2 < 3$) for the DEM calculation as described above. To establish limits on the low cutoff energy, for each time interval we iteratively fit the DEM plus `thick2` model for fixed values of the cutoff E_c ranging from 5 to 30 keV. We then examined curves of the goodness of fit parameter, χ^2, to establish lower and upper limits on E_c.

4. RESULTS FOR INDIVIDUAL TIME INTERVALS

Figure 7 plots χ^2 from the DEM+non-thermal fits as a function of the cutoff energy E_c, for the 2011 February 13 flare. For this time, early in the flare, we have a pretty good result, and it is easy to identify upper and lower limits for the cutoff energy. This χ^2 curve shape was typical for most of the intervals analyzed, where for coronal abundances the lower limit is generally 5–7 keV and the upper limit is usually in the 8–10 keV range, and for photospheric abundances the limits are generally in the 15–18 and 18–25 keV ranges, respectively. These limits are determined by identifying the E_c values where the (non-reduced) χ^2 is less than 6.63 above its minimum value, which corresponds to the 99% confidence limit for the χ^2 distribution (Press et al. 1992). Figure 8

shows how the total χ^2 comprises the individual values for EVE and *RHESSI*.
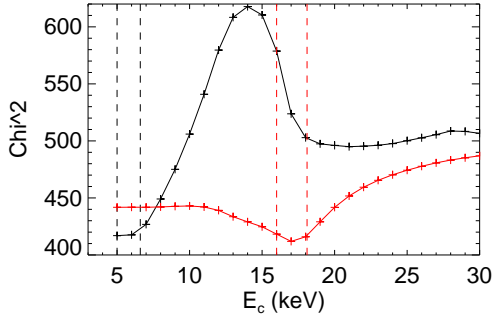
Figure 7. χ^2 vs. low cutoff energy E_c for the time interval in Figure 5, for coronal (black) and photospheric (red) abundances. Vertical dashed lines denote upper and lower limits for E_c, defined as the points on the curve where $\chi^2(E_c)$ passes through $min(\chi^2)+6.63$, corresponding to the 99% confidence limit for the χ^2 distribution.
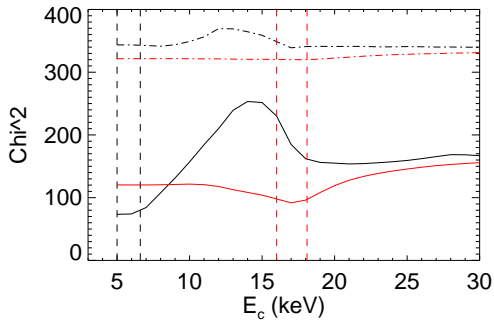
Figure 8. χ^2_{RHESSI} and χ^2_{EVE} vs. low cutoff energy E_c for the time interval in Figure 7, for coronal (black) and photospheric (red) abundances. The solid lines show the *RHESSI* components, while the dash-dot lines show the EVE components.

As can be seen from Figure 8, variation in χ^2_{RHESSI} is much larger than that for χ^2_{EVE} so that most of the "badness" for high E_c is in the *RHESSI* spectrum, as would be expected since *RHESSI* is sensitive to both the thermal *and* non-thermal changes caused by a change in E_c. Note that the values of χ^2_{RHESSI} and χ^2_{EVE} shown in Figure 8 are components from the combined fit, and not from fits to the spectra of the individual instruments, and are therefore not independent. In this case the "badness" of the *RHESSI* spectral fit for some values of E_c affects the fit to the EVE data, again expected from the joint nature of the fit.

It is instructive to examine the residuals of the spectral fits to better understand why a "bad" fit is bad, beyond just looking at χ^2 values. Figure 9 compares the *RHESSI* count spectra for the best fit E_c value (assuming coronal abundances)

of 7 keV (red) with a poorly-fit value of 16 keV (blue). For the too-high cutoff, the model spectrum does not fit the data well in the energy range of 10–20 keV. Since the high cutoff value restricts how much non-thermal emission can be included in this range, the fit procedure tries to replace this with thermal emission. This, in turn results in too many counts in the ~6.7 keV Fe line complex which is very sensitive to high temperatures. In this manner, the amount of emission seen by *RHESSI* in the Fe line limits the allowable amount of high-T emission measure. The requirement of fitting the EVE spectrum determines the amount of low-T emission measure. Thus, there must be a substantial amount of non- thermal emission in the 10–20 keV range, and this brackets the allowable E_c values. The strong influence of the Fe line complex also explains the sensitivity of the best-fit E_c value on the assumed abundances: photospheric abundances yield lower line fluxes for a given temperature compared to (higher) coronal abundances, hence requiring more emission measure and/or higher temperatures and therefore more overall thermal emission, pushing best-fit E_c values higher.

As mentioned earlier, the spectral fits to the *RHESSI* data allow for a break in the non-thermal electron power law. We have also processed the data using a non-thermal spectrum that is a single power law, without a break. It turns out that the results are similar for the two different kinds of power-law spectra for most, but not all, intervals. In particular, approximately one-sixth (9/61) of the intervals fit the data much better using the broken power-law spectrum. This is illustrated in Figure 10, for a time interval during the X flare of 15 February 2011. In this case, the broken power-law spectrum is a much better fit because it allows for an upward break in the photon spectrum. The two fits have similar power-law indices above 25 keV; for the single power law the spectral index is 5.95. For the broken power law, the spectral index is 5.45 above 13 keV and 7.75 between 7 and 13 keV. As can be seen from the figure, the broken power law fits the data much better, particularly for the energy range near 10 keV. This upward break occurs for all of the time intervals for which the broken power law result differs substantially from the single power law.

Thick-target spectra with such breaks (especially upwards) are not typically considered in flare modeling, and it is not clear what acceleration mechanism would result in such a spectrum. For example, it is possible that an upward break is due to an extra component of not necessarily thick-target electrons with a high temperature $T_{electron} > T_{ion}$ which would not be considered by a DEM calculation based mostly on ion line emission. Distinguishing such a component from the standard non-thermal component would require a much more sophisticated modeling effort that is beyond the scope of this work. Here we will stay with the use of the broken power law
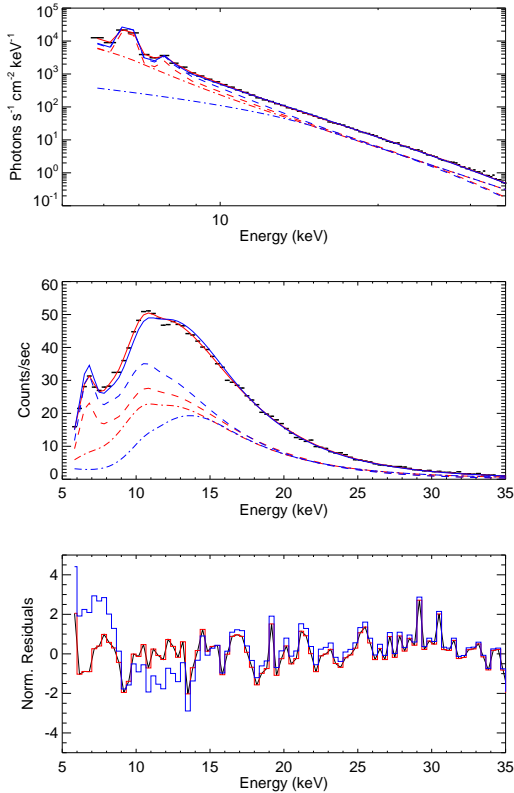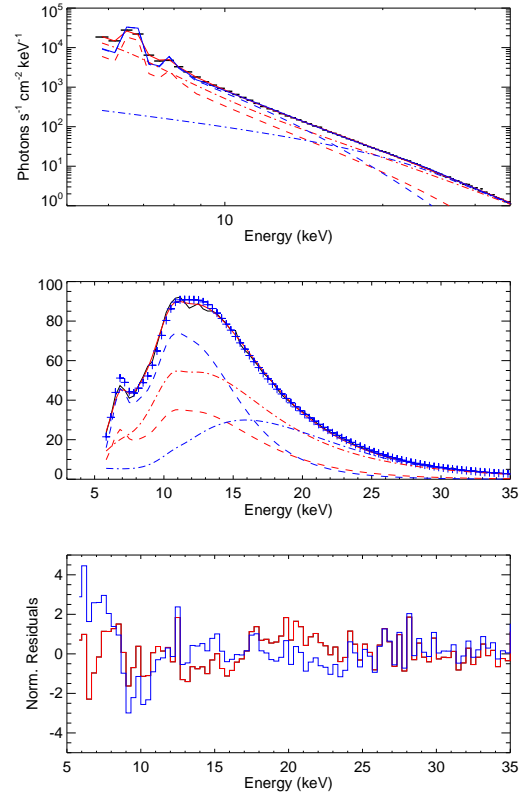
Figure 9. Top: *RHESSI* photon spectra (black) for 2011 February 13, 17:32:36 UT, with two model fits: best-fit model with E_c of 7 keV (red), and a poorly-fit model with E_c of 16 keV (blue). Dash and dash-dot lines for each color denote the thermal and non-thermal contributions, respectively. Middle: count-rate spectra corresponding to above. Bottom: normalized residuals for the two spectral models.

Figure 10. Top: *RHESSI* photon spectra (black) for 2011 February 15, 01:48:12 UT, with two model fits: best-fit broken power-law model with E_c of 7 keV (red), and best-fit single power-law model with E_c of 26 keV (blue). The broken power-law model fits better in this case. Dash and dash-dot lines for each color denote the thermal and non-thermal contributions, respectively. Middle: count-rate spectra corresponding to above. Bottom: normalized residuals for the two spectral models.

for the non-thermal spectra as this is the *simplest functional form that fits the data well for most of the flare time intervals.*

Since the analysis depends on observed counts in the Fe line complex, it is possible for results to be affected by abundance variations. Although analysis of EVE flare spectra has suggested a nearly photospheric composition for most studied events (Warren 2014), analysis of other data has yielded different results (e.g., Dennis et al. 2015; Doschek & Warren 2017), and this long-standing issue is still far from resolved. In Figure 7, the red lines show the χ^2_{RHESSI} curve and E_c limits that result if we do the calculation using photospheric abundances, where the Fe abundance is approximately 4 times smaller than in the coronal case; the E_c limits derived this way are higher.

The reason for this can be explained with the help of Figure 11. This shows the ratio of thermal photon flux for photospheric abundance and for coronal abundance for unit emission measure at 20 MK. For the Fe line emission in the 6–7 keV range, the ratio is approximately 0.3, reflecting the difference in Fe abundance. The continuum, however, is far

less sensitive to abundance variations since it includes a significant contribution from hydrogen-dominated bremsstrahlung, in addition to heavier ion-dominated radiative recombination (White et al. 2005); thus, for example, at 10 keV, the ratio is only 0.6, twice as large as for the Fe line. So, for photospheric abundance, the ratio of Fe line emission to 10-keV continuum is approximately 1/2 the value as for coronal abundance, requiring higher model temperatures to fit the same observed line-to-continuum ratio, resulting in more thermal emission at higher temperatures and consequently higher fit values for E_c. The small values of line to continuum ratio that can be inferred from Figures 9 and 10 are fully consistent with a substantial amount of thermal emission in the range above 10 keV, when assuming photospheric abundances, thereby raising the cutoff energy under that assumption.

In Figure 7 the minimum value of χ^2 is smaller for photospheric abundance, but the difference between the two minima ($\Delta(\chi^2) = 5$) is small. For most time intervals (45 of 61),
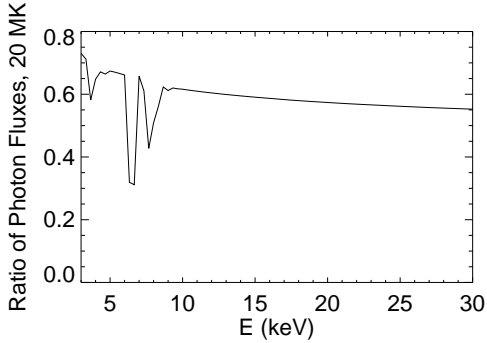
Figure 11. The ratio of thermal photon fluxes for photospheric and coronal abundances for $T = 20$ MK.

however, the minimum χ^2 value for coronal abundance is slightly smaller than that for photospheric abundance. (This can be seen from values for *reduced* χ^2 are shown in table 1.)

In future work we will include elemental abundances as fit parameters which can vary during processing, with the object of deriving rather than assuming the relative abundance values.

5. RESULTS FOR THE FULL SAMPLE

Table 1 is a comparison of the cutoff values and limits from the EVE-*RHESSI* DEM models. The table columns show: interval date and time; derived limits for low cutoff energy E_c and for the total integrated electron energy flux $\mathcal{E}_t$, using coronal and photospheric abundances; the difference between the values of $\mathcal{E}_t$ at the best-fit E_c and with $E_c = 15$ keV (for reference); values of *reduced* χ^2 for coronal and photospheric abundances (all of which are reasonably small); the ratio $R(Fe)$ of the *RHESSI* count rate in the ~ 6.7 keV Fe line complex to the peak of the count rate in the 10–12 keV range (see the middle panel of Figure 9, that shows the two peak structure in the *RHESSI* count spectrum); and the ratio $R_f(Fe)$ of the photon fluxes in these same energy ranges. A value of "NA" for $R(Fe)$ means that there was no separate peak in the count spectrum (because the thin attenuator was not engaged at that time), and we are unable to calculate that count ratio (the photon flux ratio $R_f(Fe)$ is always well defined, but we like to use the counts ratio when possible because it is not model dependent).

For most of the examined intervals, we managed to get limiting values for E_c. For 10 of the 61 intervals, the χ^2 curve using coronal abundances was flat or bi-modal, with a difference between high and low E_c limits greater than 15 keV, so there are 51 good sets of derived limits. Using photospheric abundances, there are 45 good sets of limits.

The 10 time intervals for which we obtained no good E_c limits with coronal abundances can be divided into three different categories. (1) Six intervals are characterized by high Fe line emission relative to the peak continuum emission in
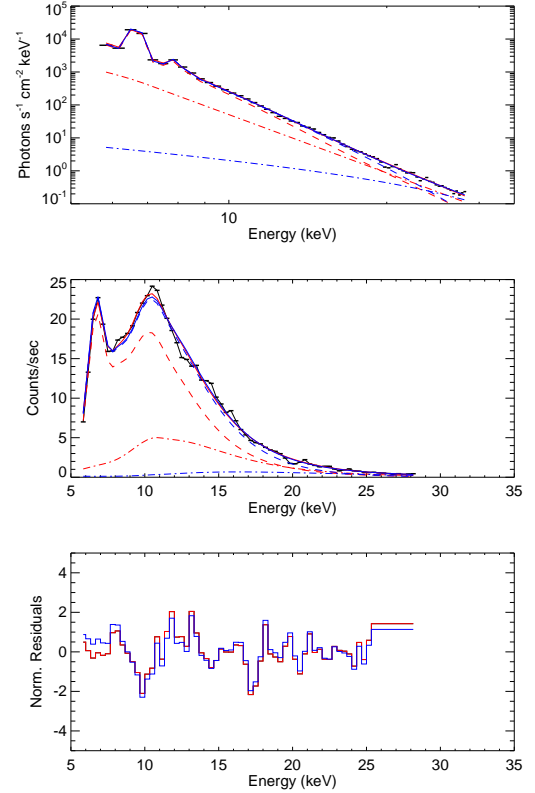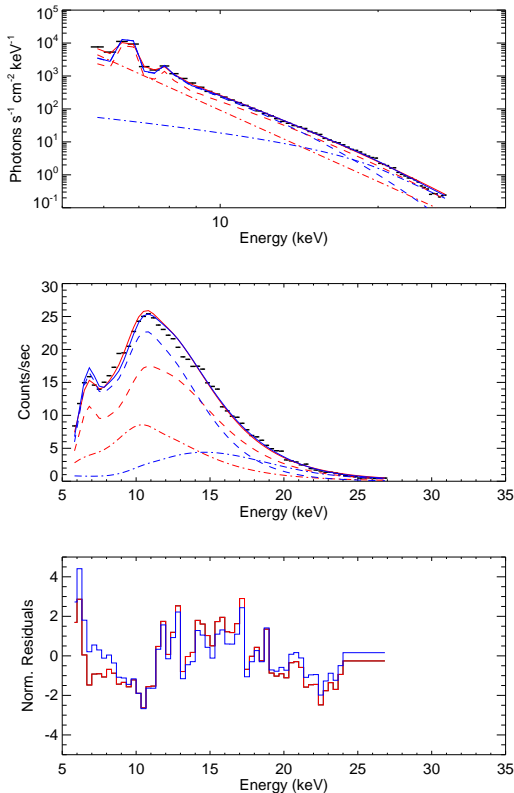

Figure 12. Top: *RHESSI* photon spectra for 2011 March 9, 13:57:40 UT, highlighting the effect of a relatively high Fe line-to-continuum ratio. Black – observed flux; red – best-fit model with $E_c = 7$ keV; blue – model with $E_c = 25$ keV. Dash and dash-dot lines for each color denote the thermal and non-thermal contributions, respectively. Middle: count-rate spectra corresponding to above. Bottom: normalized residuals for the two spectral models. Despite the significant difference in E_c, the two model photon spectra are nearly identical.

the 10–12 keV range ($R(Fe) \gtrsim 1$), as shown in Figure 12 and in Table 1. These tend to have very flat spectra below a break energy E_{br} and above the cutoff value E_c, so the spectral shape does not strongly constrain E_c and the resulting photon spectra for low and high E_c values are similar. (2) Two are bi-modal in χ^2, and for low E_c values the best-fit non-thermal component is a very steep spectrum that offsets the higher-T emission measure required by a high E_c, as shown in Figure 13. (3) For the remaining two times, there is no obvious pattern in the spectra or fitting behavior to indicate why we cannot obtain a limit from the χ^2 curve. Similar patterns for photospheric abundance are not obvious.

Figure 14 shows histograms of derived cutoff energies. For coronal abundance, most of the E_c lower limits (39 of 51) are less than 10 keV, and many of these intervals (32 of 51) have E_c lower limits of 5 keV, in the range where *RHESSI* begins to lose sensitivity (Smith et al. 2002). For those cases, the lower limit may be less than 5 keV since we do not include

Figure 13. Top: *RHESSI* photon spectra for 2011 September 6, 01:37:36 UT; for low E_c values a very steep non-thermal component offsets the higher-T emission measure required by a high E_c. Black – observed flux; red – best-fit model with $E_c = 5$ keV; blue – model with $E_c = 21$ keV. Dash and dash-dot lines for each color denote the thermal and non-thermal contributions, respectively. Middle: count-rate spectra corresponding to above. Bottom: normalized residuals for the two spectral models. Despite the significant differences in the thermal and non-thermal contributions for the two values of E_c, the total spectra and χ^2 values for the two cases are similar.

RHESSI data below 5 keV in processing. In contrast, for photospheric abundance only 8 intervals have E_c below 10 keV.

For coronal abundance, one-half of the intervals (26 of 51) have both upper and lower E_c limits at or below 10 keV. Only a few (12) intervals for coronal abundance have E_c lower limits above 10 keV. In comparison, for photospheric abundance, most intervals (30 of 45) have E_c upper limits between 15 and 25 keV, and most (36 of 45) also have lower limits for E_c above 10 keV.

6. DISCUSSION AND CONCLUSIONS

We have shown that the *RHESSI*+EVE DEM model generally yields values for upper and often though less frequently) lower limits to the non-thermal low cutoff energy E_c, early in flares when the thermal emission does not overwhelm the non-thermal component. When assuming coronal abundances, these derived cutoff energies are typically low, below
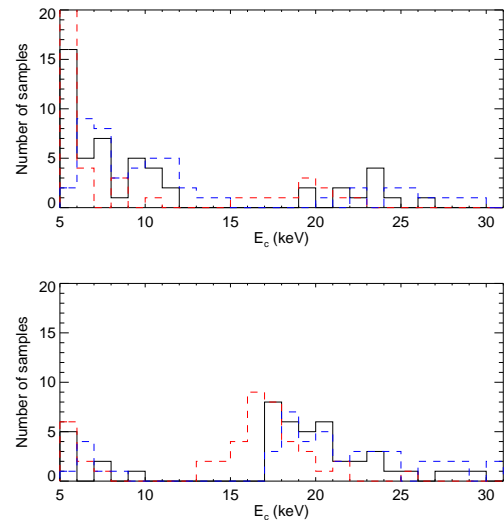

Figure 14. Top: Histograms of best-fit (black), and lower (red) and upper (blue) limits, for the low-energy cutoff E_c for the 51 time intervals with discernible limits using coronal abundances. Bottom: as above, for the 45 time intervals with good limits using photospheric abundances.

10 keV, with most values of the lower limits in the 5–7 keV range and upper limits below 20 keV. For photospheric abundances, the E_c values are typically ∼10 keV higher.

For most of the analyzed time intervals, upper limits for E_c can be obtained because the amount of high-T emission measure is strongly constrained by the flux observed in the ∼6.7 keV Fe line complex. For time intervals with a relatively large amount of Fe line emission relative to the adjacent continuum, however—roughly 1/6th of the sample—the spectral shape is also much flatter and the Fe line is less constraining, and we do not obtain good limits for E_c in those cases. Note that these "high-Fe" flares exhibit significant high-T components at the start of the hard X-ray emission, and thus do not fit in well with the standard flare model interpretation of thermal plasma being the result of "chromospheric evaporation" driven by energy deposition from non-thermal electrons. These may be examples of *in-situ* heating as discussed by, e.g., Caspi & Lin (2010), Longcope & Guidoni (2011), and Caspi et al. (2015a).

When we measure E_c, we are actually measuring *the energy at which an assumed non-thermal photon spectrum is forced to have a downwards break due to the presence of thermal emission.* We chose the thick-target model with a sharp cutoff for this work both for convenience and because it is well defined and commonly used and accepted in the community. We obtain similar results using a more physically realistic thick-target electron model which has a flat electron spectrum below E_c (e.g., Saint-Hilaire & Benz 2005)). We have reprocessed the sample times using a model with a flat spectrum below E_c and typically find only a 1–2 keV differ-

ence between limits obtained using this flat cutoff model and the nominal sharp cutoff model, for most flares and particularly for those with low E_c values. This is because the photon spectra for the two different models do not differ very much in the few keV just below E_c. This can be seen in Figure 2, where we compare the spectra for the sharp and flat cutoff cases. Since the low-cutoff flares have upper limits from 7 to 10 keV, and the models are only fit above 5 keV, we should not expect to see much difference. For example, in Figure 15, we compare the χ^2_{RHESSI} curve for a sharp cutoff to that for a flat cutoff, and the difference in the upper limit found is 1 keV, with no difference in lower limit. For the full sample of flares, the difference between the best fit E_c for the flat cutoff and for the sharp cutoff is less than 2 keV for 51 of 61 intervals for coronal abundances.
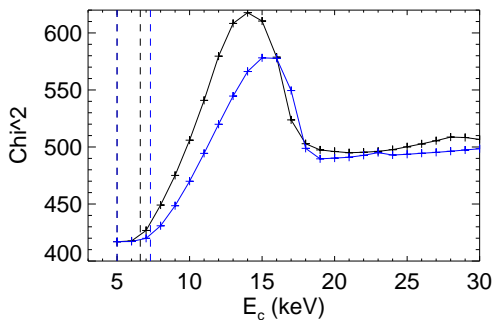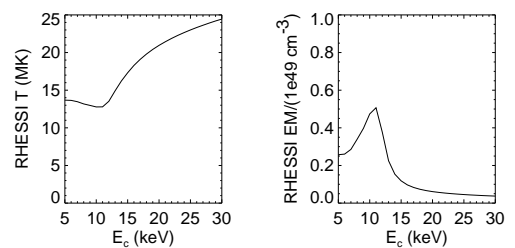

Figure 15. χ^2_{RHESSI} vs. low cutoff energy E_c for the time interval 2011 February 13, 17:32:36 UT, for a sharp (black) and flat (blue) cutoff. Dashed lines denote upper and lower limits for E_c. The flat cutoff model has an upper limit for E_c about 1 keV greater than the sharp cutoff model.

We have also tested thin-target electron models and *ad hoc* (empirical) sharply-broken power-law photon spectra with photon spectral index below a given E_c fixed at 1.5 (as has been commonly used in prior studies) versus the $\sim$1.8 and $\sim$2.1 gradual rollovers seen from the f_thick2 models shown in Figure 2. We obtain similar results for the thin-target and *ad hoc* models as for the nominal thick-target case.

The main conclusion to take away from this work is that, for most of the flares in the sample, it is possible to obtain limits on E_c early in the flare. Values are relatively low ($<$10 keV) for coronal abundance because the amount of emission observed in the $\sim$6.7 keV Fe line complex limits the amount of high-T emission measure, and therefore limits the thermal continuum contribution to the energy range above 10 keV. These results are not very dependent on the details of the non-thermal model and should be valid for *any* model with a cutoff in the electron distribution, or that requires a relatively flat photon spectrum below an energy E_c.

Ours are lower limits than have been determined in past calculations using *RHESSI* data, such as by Saint-Hilaire & Benz (2005) or Sui et al. (2007), which are typically above 15 keV. We obtain similar E_c values, above 15 keV, when using photospheric abundances.

We can see how these low values of E_c for coronal abundance might arise by examining just the *RHESSI* data. In a similar procedure to the EVE-*RHESSI* DEM calculations, we fit RHESSI isothermal plus thick-target spectra for each value of E_c from 5 to 30 keV. Figure 16 shows the fit T and *EM* for these isothermal plus thick-target spectra as a function of E_c for the time interval in Figure 5. Figure 17 shows a plot of the value of reduced χ^2 output by the Solarsoft OSPEX fitting package. From Figure 16, we see that as the assumed E_c increases, the best-fit model T also increases, up to 25 MK. As discussed previously, this is expected, since higher-T emission is required by the reduction in non-thermal emission from increased E_c. From Figure 17, we see that the χ^2 curve, the black line, is relatively flat, so that the "correct" value of E_c is not strongly distinguished by the chi^2 statistic with *RHESSI* data alone. This is unlike the χ^2 curves for most of the EVE-*RHESSI* DEM models. The red curve shown in Figure 17 is for RHESSI spectral fits for which we have restricted the temperature to be less than 1.2 keV, or 14 MK, the best-fit T value for E_c = 5 keV from Figure 16. For those spectra, we reproduce a χ^2 curve that is similar to the EVE-*RHESSI* DEM case. We can conclude that we find low values of E_c using both EVE and *RHESSI because the need to fit both instruments simultaneously results in a DEM curve that has a much lower average temperature (in the 10–15 MK range) than might be inferred from RHESSI alone.*

Figure 16. Best-fit temperature T (left, in MK) and emission measure *EM* (right, in 10^{49}cm^{-3}) values for isothermal *RHESSI* spectra as functions of low cutoff energy E_c for 2011 February 13, 17:32:36 UT.

It has been pointed out that, when interpreted as due to cold thick-target emission, relatively low values of E_c imply very large values for the non-thermal electron flux needed to account for the observed emission, i.e., the so-called "number problem" (Benz 2017). This remains true here for the coronal abundance cases: in the sixth column of Table 1, we show
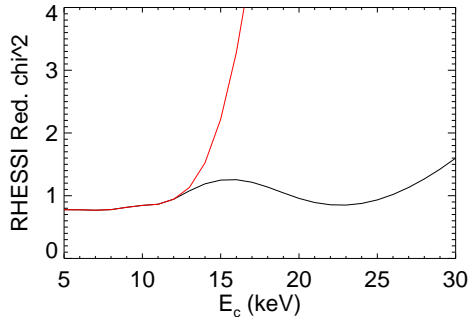
Figure 17. Values of reduced χ^2 for isothermal *RHESSI* spectra as functions of low cutoff energy E_c for 2011 February 13, 17:32:36 UT. The black line shows values for spectral fits for which the temperature was unrestricted, as in Figure 16. The red line shows values for spectral fits for which the temperature was capped at 14 MK.

$Log(\mathcal{E}_{diff})$, the difference between the amount of total electron energy flux $\mathcal{E}_t$ required for the best-fit value of E_c, and the amount of energy flux for $E_c = 15$ keV. For 37 of the 61 samples, this value is greater than 1.0 (i.e., we require more than an order of magnitude more electron energy than for the 15 keV cutoff).

Assuming photospheric abundances would appear to mitigate this "number problem", as the resultant E_c values are higher, thus requiring significantly less total non-thermal energy. This assumption would seem to be supported by prior studies such as Warren (2014), but other studies, such as Dennis et al. (2015), suggest that coronal abundances may be more appropriate, so there is no clear distinction between one choice versus the other. As noted previously, the higher E_c values determined with photospheric abundances are also more consistent with prior studies of *RHESSI* data alone, such as Sui et al. (2007), but those studies used isothermal approximations to the thermal emission and could not consider the additional constraints on the thermal parameters afforded by requiring a simultaneous fit to a different instrument with different temperature sensitivity (in our case, EVE). We also note that fewer intervals were well fit under the photospheric abundance assumption, in part because the χ^2 appears to be less sensitive to E_c under this assumption, as is clear from the red curves in Figures 7 and 8.

Other physical considerations may help to mitigate this "number problem" besides the choice of abundances, as well, such as consideration of more realistic non-thermal models including, for example, return current (Zharkova et al. 1995) or "warm-target" plasma (Kontar et al. 2015, 2019). Many of our lower E_c limits of 5–7 keV are only a few times greater than the temperatures of 10–30 MK (equivalent to approximately 1–3 keV) that we obtain in the DEM calculation, suggesting that a warm-target model may be most appropri-

ate. We can make direct comparisons with results for some of the flares that we have analyzed with results shown by Aschwanden et al. (2016), albeit for different time intervals. For example, in that work, the 2011 February 13 flare that we have been using for demonstration is shown to have a "warm-target" cutoff of 8.3 keV. This is close to the limits that we obtain here, using a vastly different calculation and more assumptions. Most of the flares analyzed in Aschwanden et al. (2016) have low (<10 keV) cutoff energies for the "warm-target" approximation, similar to our results here.

As noted above, the original DEM model discussed by Caspi et al. (2014b) separately fit the Fe and Fe-Ni line complexes (at ∼6.7 and ∼8 keV), and did not use the CHIANTI package for those lines. This stemmed from suggestions by Phillips et al. (2006) and Caspi & Lin (2010) that the ionization fraction versus temperature for the Fe line complex may not be quite correct, based on analysis of *RHESSI* results. For this work, however, it is absolutely necessary to include the Fe line emission as modeled by the CHIANTI package, rather than fitting it separately, since tying the lines and continuum together provides the ability to constrain the high-T emission measure and subsequent thermal continuum emission model. We use the default CHIANTI ionization fraction model, as implemented in CHIANTI version 7.1.3 (Landi et al. 2013).

For most of the flares in the sample, we were able to attempt the calculation for both of the first two one-minute intervals during the start of flare. This added an extra level of validation in those cases; if the limits on E_c are not at least similar for the two time intervals in the same flare, and/or there is some systematic difference between the other model parameters for the two intervals, then we might suspect our calculations. Note that each calculation is independent for each interval; we do not use the common practice of relating the initial conditions for a subsequent time interval to those from the previous time interval in a given flare. For coronal abundances, for 18 of 22 flares for which good fits were obtained for both intervals, the limits overlap. This suggests that E_c may be relatively stable on the scale of minutes, but in the absence of good limits over the entire evolution of multiple flare impulsive phases, we hesitate to draw a general conclusion.

It is important to note that, since we are looking at time intervals early during flares, the Fe XXV ions mostly responsible for the ∼6.7 keV line complex may not be in equilibrium, i.e., the ion population may not fully reflect the balance of ionization states expected from the temperature distribution. The equilibrium time scale is dependent on the density of the hot plasma. Simple order-of-magnitude estimates for the high-temperature plasma density based on the size of the *RHESSI* image and the high-T emission measure (cf. Caspi 2010; Caspi et al. 2014b) give densities of order 10^{9-11} cm^{-3},

as shown in Table 2. Phillips (2004) suggested that for densities of 10^{10} cm^{-3} or less, the ionization equilibrium may be problematic. However, we believe that ionization equilibrium is mostly attained since, for most of the flares, the ratios of counts and photon flux for the Fe line complex to the 10–12 keV continuum, $R(Fe)$ and $R_f(Fe)$, remain relatively stable from minute to minute during the flares for which we fit two intervals, as can be seen in Table 2. (Note that this sample contains time intervals for which we had no good E_c limits). For 15 of 22 of these flares, the ratio $R_f(Fe)$ varies by less than 50%. This would not be the case if the Fe XXV ionization had to "catch up" over time.

Table 2 shows the results for the flares for which we have two measurements, for high-T emission measure EM_{16} (the integral of the DEM for all $T > 16$ MK), volume V_{16}, density N_{16}, ionization time scale $\tau_{Fe\text{XXV}}$, and heating time scale, τ_{HEAT}. The ionization time scale $\tau_{Fe\text{XXV}} = 1/(N \times Q)$, where Q is the ionization rate for Fe XXIV to Fe XXV (Jordan 1970; Phillips 2004). The value of Q depends on temperature; for this case, since we are integrating over "all" high-T, we used an average of the values for $T = 10^{7.2–7.5}$, or $Q = 10^{-11.12}$. The heating time scale is given by $\tau_{\text{HEAT}} = ((1/EM_{16}) \times \delta(EM_{16})/\delta t)^{-1}$.

For all of the flares in the sample $\tau_{Fe\text{XXV}}$ is less (usually much less) than τ_{HEAT}, consistent with prior studies of early-flare emission (e.g., Caspi & Lin 2010) and again suggesting that non-equilibrium ionization is not an issue for these events. The plasma density N_{16} would have to be an order of magnitude lower for the ionization scale $\tau_{Fe\text{XXV}}$ to be as long as the heating time scale τ_{HEAT}.

The calculation that we have done here for E_c is as comprehensive as we can get considering the available instrumentation. For future work it would be useful to have good observations of high-T line emissions that can be separated from the need to account for the non-thermal continuum, so that the entire thermal X-ray continuum can be estimated independently and subtracted, yielding the expected non-thermal component directly. The *Yohkoh* Bragg Crystal Spectrometer, with Ca XIX, Fe XXV, and Fe XXVI channels, is a good example of one such instrument useful for DEM analysis (Culhane et al. 1991; McTiernan et al. 1999). Soft X-ray spectra from, e.g., the *Miniature X-ray Solar Spectrometer* (*MinXSS*; Mason et al. 2016; Moore et al. 2018) CubeSat, will provide additional diagnostics of the DEM and abundances for a number of elements (e.g., Caspi et al. 2015b; Woods et al. 2017). Combining *MinXSS* data with that from other instruments, particularly *RHESSI*, will open new areas of parameter space to further constrain E_c in different ways.

APPENDIX: CALIBRATION NOTES

For comparison purposes, it is useful to calculate results for the individual instruments. As shown by Caspi et al. (2014b), we find good agreement between EVE and *RHESSI*, individually, in the temperature range of 10–20 MK where both instrument responses overlap. Here we compare EVE and *RHESSI* during the decay phase of some flares during February 2011. The EVE and *RHESSI* data are first fit separately (in contrast to the situation discussed regarding Figure 8, where χ^2_{RHESSI} and χ^2_{EVE} are separate components of a combined fit). The individual DEM functions are then compared with the DEM from the combined fit. In Figure 18 we show the DEM for the interval 2011 February 16, 14:40:44 UT to 14:41:44 UT, for each instrument individually and for the combined instruments. The red curve, for *RHESSI*, and black curve, for EVE, are similar in the range $Log(T)$ of 6.5 to 7.4. The blue curve, for the combined instruments, stays with the EVE curve at low T and the *RHESSI* curve at high T.
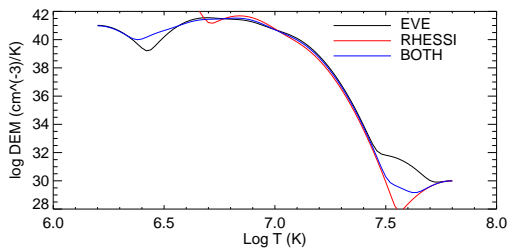
Figure 18. DEM curves for EVE (black), *RHESSI* (red), and EVE+*RHESSI* (blue) for the time interval 2011 February 16, 14:40:44 UT to 14:41:44 UT, when no *RHESSI* attenuators were engaged.

Figure 18 shows an interval for which the *RHESSI* attenuators were out. Most of the intervals that we have looked at in this work, however, have the thin attenuator in. Figure 19 shows the DEM for an attenuator-in interval, for 2011 February 13, 17:50:32 UT to 17:51:32 UT. Here the EVE and *RHESSI* curves are similar in the range $log(T)$ of 7.0 to 7.4, with the combined solution again following the EVE curve at low T and *RHESSI* at high T, with a "crossover" point, where the individual EVE and *RHESSI* curves match at $log(T) = 7.1$.

Figure 19 highlights the need to consider the combination of both EVE and *RHESSI* due to the poor results at either end of the temperature range when considering the instruments individually. This is typical behavior, as shown in Figure 20. Here we show 10 different comparisons, for two sets of five 1 minute intervals during the decay phases of flares on 2011 February 13 and 15. To remove time dependence in this comparison, for each set of EVE, *RHESSI* and EVE+*RHESSI* solutions, we normalize so that the EVE curve passes through
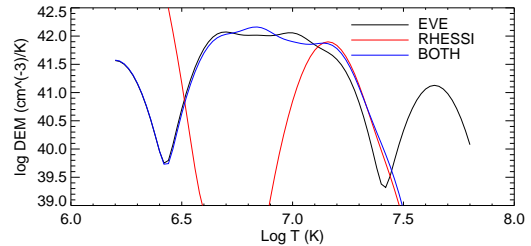
Figure 19. DEM curves for EVE (black), *RHESSI* (red), and EVE+*RHESSI* (blue) for the time interval 2011 February 13, 17:50:32 UT to 17:51:32 UT, when the *RHESSI* thin attenuator was engaged.

the same point at $Log(T) = 7.1$. For all of these solutions, the combined (blue) curve matches well with EVE at low T, with *RHESSI* at high T, and with both in the middle. The high $log(T) = 7.6$ component (40 MK) that often appears in the EVE solutions is suppressed when *RHESSI* is included, and the low $Log(T) < 6.7$ component (5 MK), for *RHESSI*, which does not reflect reality, is likewise suppressed when EVE is included.
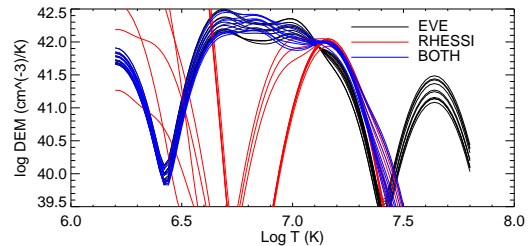
Figure 20. Multiple DEM curves for EVE (black), *RHESSI* (red), and EVE+*RHESSI* (blue) for 10 different one minute time intervals in the ranges of 2011 February 13, 17:50:32 UT to 17:55:32 UT and 2011 February 15, 02:15:48 UT to 02:20:48 UT. For each time interval, for purposes of comparison, the three solutions are normalized so that the EVE DEM is the same at $Log(T) = 7.1$.

Warren et al. (2013) found good agreement between the EVE and *GOES* XRS instruments. We can do a similar comparison here. In Figure 21 we compare estimates of *GOES* fluxes (black lines) from DEM models including EVE plus *GOES*, as in Warren et al. (2013) (red), and EVE+*RHESSI* (blue). The EVE+*RHESSI* DEM underestimates the *GOES* emission by a factor of approximately 2. This may be due to a loss of sensitivity for *RHESSI* later during the mission, as discussed by McTiernan (2009a).

To investigate this, Figure 22 shows a different sort of *RHESSI*-to-*GOES* comparison. The left-hand plot shows the photon flux for a *RHESSI* spectral fit for an interval from the decay phase of an X-flare for the time interval 2011 February 13, 17:50:32 UT to 17:51:32 UT. The right-hand plot is the same comparison for the time interval 2002 July 23,
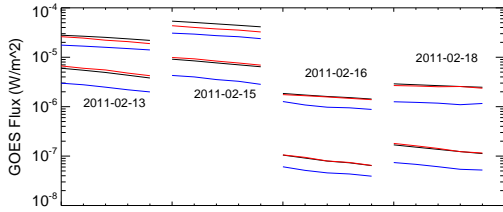
Figure 21. Comparison of *GOES* flux (W m^{-2}) estimates for DEM models calculated using EVE and *GOES* (red), and EVE and *RHESSI* (blue) during the decay phases of four flares during February 2011, compared with measured values (black). The time intervals are: 2011 February 13, 17:50:32 UT to 17:55:32 UT; 2011 February 15, 02:15:48 UT to 02:20:48 UT; 2011 February 16, 14:38:44 UT to 14:43:44 UT; and 2011 February 18, 13:15:00 UT to 13:20:00 UT.

01:05:00 UT to 01:06:00 UT when the *RHESSI* detectors were at full sensitivity. In each plot the red line is the expected photon flux from a *GOES* temperature measurement for the same time interval. The *RHESSI* spectrum was fit using the same procedure as Caspi & Lin (2010), and the *GOES* spectrum was calculated using the SolarSoft IDL software package. As can be seen, relative to the *GOES* flux, the *RHESSI* flux is less for the later time interval. We have done this comparison for all of the four time intervals shown in Figure 21. For the first two (with attenuator state in), for 2011 February 13 and 15, we compare with five one minute time intervals from 2002 July 23, 01:05:00 UT to 01:10:00 UT. The 2002 July 23 intervals were chosen to have similar *RHESSI* and *GOES* temperature values to the 2011 February 13 and 15 intervals. For non-attenuated 2011 February 16 and 18 times, we compare with 2002 July 26, 00:37:00 UT to 00:42:00 UT. For each interval, we calcu-
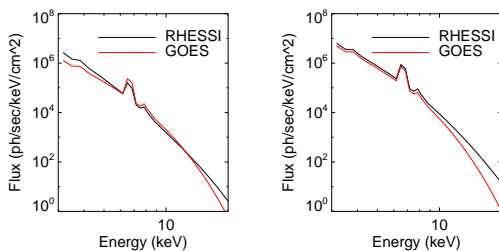

Figure 22. Comparison of photon flux (photons s^{-1} cm^{-2} keV^{-1}) for *RHESSI* spectral fits (black) as in Caspi & Lin (2010) with photon flux inferred from *GOES*-derived T and EM values (red) calculated via SolarSoft, for 2011 February 13, 17:50:32 UT to 17:51:32 UT (left) and 2002 July 23, 01:05:00 UT to 01:06:00 UT (right).

lated the ratio of *RHESSI* flux to *GOES*-derived flux in the range between 6 and 10 keV. For the 2002 July 23 time interval, we found the ratio to be 1.36, i.e., the *RHESSI* flux is a

factor of 1.36 greater than the flux calculated from the *GOES* temperature and emission measure; for the 2011 February 13 and 15 time intervals, the ratio is 0.78. Thus, in 2011 *RHESSI* seems approximately 0.57 as sensitive as in 2002. The change in ratio is similar for the non-attenuated case; for 2002 July 26 the ratio is 3.11, while for the 2011 February 16 and 18 flares the ratio is 1.77, again showing a relative sensitivity of 0.57. Note also that extending the calculations done by McTiernan (2009a) for the full mission estimates a loss of sensitivity of approximately 0.70.

To attempt to include this sensitivity loss in the combined EVE+*RHESSI* calculations, we multiply the nominal *RHESSI* detector response by a factor of 0.5, reducing *RHESSI* sensitivity by a factor of 2 for the 2011 February 13 and 15 time intervals. We find that while the values of χ^2 are not as good for the reduced-sensitivity solutions, there is not much change in the fit values of cutoff energy E_c. In Figure 23 we show the χ^2 curves for the time interval 2011 February 13, 17:32:36 UT for the reduced-sensitivity case. In Figure 24 we reproduce Figure 7 for comparison. As can be seen, the values for the limits on the cutoff energy E_c do not change by much. This is a much smaller effect than the effect of changing abundances as shown in the paper; hence we did not test or adopt the reduced-sensitivity model for the full sample of flares. It is possible that a change in sensitivity that is energy-dependent may change the E_c result, but we currently have no good way to test this.
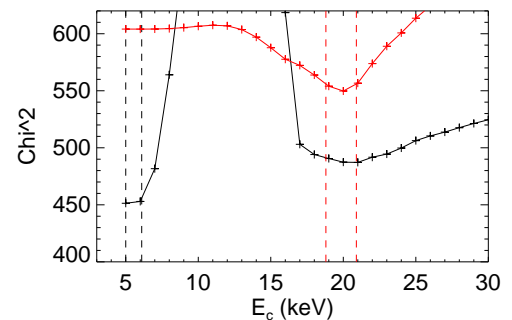
Figure 23. χ^2 vs. low cutoff energy E_c for the time interval in Figure 5, for the reduced-sensitivity models. Dashed lines denote upper and lower limits for E_c. For coronal abundance (black) the reduced-sensitivity model has an upper limit for E_c about 0.5 keV less than full sensitivity model. For photospheric abundance, the reduced sensitivity model changes the E_c limits by about 3 keV.
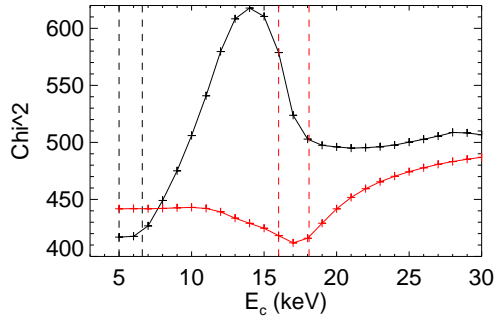
Figure 24. χ^2 vs. low cutoff energy E_c for the time interval in Figure 5, for coronal (black) and photospheric (red) abundances. Vertical dashed lines denote upper and lower limits for E_c, defined as the points on the curve where $\chi^2(E_c)$ passes through $min(\chi^2)+6.63$, corresponding to the 99% confidence limit for the χ^2 distribution.

REFERENCES

Aschwanden, M. J., Holman, G., O'Flannagain, A., et al. 2016, ApJ, 832, 27

Benz, A. O. 2017, Living Reviews in Solar Physics, 14, 2

Brown, J. C. 1971, SoPh, 18, 489

Caspi, A. 2010, PhD thesis, Department of Physics, University of California, Berkeley, CA 94720-7450, USA

Caspi, A., Krucker, S., & Lin, R. P. 2014a, ApJ, 781, 43

Caspi, A., & Lin, R. P. 2010, ApJL, 725, L161

Caspi, A., McTiernan, J. M., & Warren, H. P. 2014b, ApJL, 788, L31

Caspi, A., Shih, A. Y., McTiernan, J. M., & Krucker, S. 2015a, ApJL, 811, L1

Caspi, A., Woods, T. N., & Warren, H. P. 2015b, ApJL, 802, L2

Culhane, J. L., Hiei, E., Doschek, G. A., et al. 1991, SoPh, 136, 89

Dennis, B. R., Phillips, K. J. H., Schwartz, R. A., et al. 2015, ApJ, 803, 67

Dere, K. P., Landi, E., Mason, H. E., Monsignori Fossi, B. C., & Young, P. R. 1997, A&AS, 125, 149

Donnelly, R. F., Grubb, R. N., & Cowley, F. C. 1977, NASA STI/Recon Technical Report N, 78

Doschek, G. A., & Warren, H. P. 2017, ApJ, 844, 52

Fletcher, L., Dennis, B. R., Hudson, H. S., et al. 2011, SSRv, 159, 19

Freeland, S. L., & Handy, B. N. 1998, SoPh, 182, 497

Haug, E. 1997, A&A, 326, 417

Hock, R. A., Chamberlin, P. C., Woods, T. N., et al. 2012, SoPh, 275, 145

Jordan, C. 1970, MNRAS, 148, 17

Kane, S. R., McTiernan, J., Loran, J., et al. 1992, ApJ, 390, 687

Koch, H. W., & Motz, J. W. 1959, Reviews of Modern Physics, 31, 920

Kontar, E. P., Jeffrey, N. L. S., & Emslie, A. G. 2019, ApJ, 871, 225

Kontar, E. P., Jeffrey, N. L. S., Emslie, A. G., & Bian, N. H. 2015, ApJ, 809, 35

Landi, E., Young, P. R., Dere, K. P., Del Zanna, G., & Mason, H. E. 2013, ApJ, 763, 86

Leach, J., & Petrosian, V. 1981, ApJ, 251, 781

Lin, R. P., Dennis, B. R., Hurford, G. J., et al. 2002, SoPh, 210, 3

Longcope, D. W., & Guidoni, S. E. 2011, ApJ, 740, 73

Mason, J. P., Woods, T. N., Caspi, A., et al. 2016, Journal of Spacecraft and Rockets, 53, 328

McTiernan, J. M. 2009a, RHESSI Science Nugget 117

—. 2009b, ApJ, 697, 94

McTiernan, J. M., Fisher, G. H., & Li, P. 1999, ApJ, 514, 472

McTiernan, J. M., & Petrosian, V. 1990, ApJ, 359, 524

Moore, C. S., Caspi, A., Woods, T. N., et al. 2018, SoPh, 293, 21

Neupert, W. M. 1968, ApJL, 153, L59

Pesnell, W. D., Thompson, B. J., & Chamberlin, P. C. 2012, SoPh, 275, 3

Phillips, K. J. H. 2004, ApJ, 605, 921

Phillips, K. J. H., Chifor, C., & Dennis, B. R. 2006, ApJ, 647, 1480

Press, W. H., Teukolsky, S. A., Vetterling, W. T., & Flannery, B. P. 1992, Numerical recipes in FORTRAN. The art of scientific computing, 2nd edn. (Cambridge, UK: Cambridge University Press)

Saint-Hilaire, P., & Benz, A. O. 2005, A&A, 435, 743

Shibata, K. 1996, Advances in Space Research, 17, 9

Smith, D. M., Lin, R. P., Turin, P., et al. 2002, SoPh, 210, 33

Sui, L., Holman, G. D., & Dennis, B. R. 2007, ApJ, 670, 862

Warmuth, A., Holman, G. D., Dennis, B. R., et al. 2009, ApJ, 699, 917

Warmuth, A., & Mann, G. 2016, A&A, 588, A115

Warren, H. P. 2014, ApJL, 786, L2

Warren, H. P., Mariska, J. T., & Doschek, G. A. 2013, ApJ, 770, 116

White, S. M., Thomas, R. J., & Schwartz, R. A. 2005, SoPh, 227, 231

Woods, T. N., Eparvier, F. G., Hock, R., et al. 2012, SoPh, 275, 115

Woods, T. N., Caspi, A., Chamberlin, P. C., et al. 2017, ApJ, 835, 122

Zharkova, V. V., Brown, J. C., & Syniavskii, D. V. 1995, A&A, 304, 284

Date_time	δt	E_c(coronal)	E_c(photo)	Log($\mathcal{E}_t$) coronal	Log($\mathcal{E}_t$) photo	Log($\mathcal{E}_{diff}$)	χ^2 coronal	χ^2 photo	$R(Fe)$	$R_f(Fe)$
20110213_173136	60.0	5.0 − 10.5	5.0 − 18.4	28.4 − 29.6	27.4 − 28.4	1.2	0.32	0.32	0.62	17.20
20110213_173236	60.0	5.0 − 6.6	16.0 − 18.1	30.4 − 31.1	28.3 − 28.5	2.6	0.68	0.67	0.61	19.41
20110215_014712	60.0	5.0 − 11.2	5.0 − 30.0	28.4 − 30.3	20.9 − 21.4	2.5	0.52	0.51	0.50	15.47
20110215_014812	60.0	5.0 − 7.3	15.2 − 18.4	30.4 − 31.2	28.5 − 28.7	1.7	0.20	0.18	0.51	13.94
20110216_142304	60.0	5.0 − 30.0	15.4 − 18.8	26.9 − 27.4	27.9 − 28.1	−0.0	0.15	0.22	0.96	24.67
20110216_142404	36.0	5.0 − 9.3	16.1 − 17.7	29.3 − 31.1	28.1 − 28.3	2.9	0.15	0.20	0.79	30.61
20110228_124644	60.0	5.0 − 11.2	5.0 − 30.0	28.6 − 29.8	26.5 − 28.2	1.5	0.58	0.56	0.47	14.06
20110228_124744	60.0	6.7 − 10.3	15.8 − 20.0	29.1 − 30.1	27.8 − 27.9	1.3	0.50	0.51	0.61	16.91
20110307_194720	60.0	5.0 − 12.1	5.0 − 30.0	28.2 − 29.8	25.6 − 25.7	2.0	0.20	0.19	0.58	21.81
20110307_194820	28.0	5.0 − 12.2	5.0 − 30.0	28.3 − 29.4	25.7 − 28.4	0.8	0.22	0.22	0.67	21.12
20110307_214644	60.0	5.0 − 7.4	5.0 − 30.0	29.6 − 30.4	26.7 − 27.6	2.1	0.92	0.86	0.54	16.54
20110307_214744	60.0	6.2 − 8.5	17.7 − 19.6	29.7 − 30.6	28.1 − 28.3	1.9	0.42	0.41	0.63	19.32
20110308_022736	60.0	5.0 − 6.8	5.0 − 21.2	30.2 − 31.0	27.8 − 30.9	2.8	0.35	0.39	0.59	21.72
20110308_181044	60.0	5.0 − 30.0	5.0 − 24.0	27.3 − 28.4	27.7 − 28.4	0.4	0.47	0.49	0.49	13.00
20110309_135740	60.0	5.0 − 30.0	16.2 − 19.1	26.1 − 29.6	27.6 − 27.8	1.1	0.43	0.57	0.94	30.72
20110309_231820	60.0	5.0 − 9.0	5.0 − 30.0	29.6 − 31.1	25.3 − 25.5	1.6	0.29	0.36	0.67	22.24
20110309_231920	32.0	22.0 − 26.5	15.6 − 21.1	28.0 − 28.5	28.6 − 28.8	−1.0	0.47	0.49	0.63	19.70
20110314_194952	60.0	5.0 − 8.1	16.7 − 18.2	29.8 − 31.1	28.4 − 28.5	1.8	0.44	0.52	0.65	21.09
20110314_195108	60.0	5.0 − 29.0	5.0 − 25.9	27.9 − 28.6	28.0 − 28.9	−1.3	0.36	0.45	0.58	23.63
20110315_002104	60.0	5.0 − 7.6	17.7 − 20.2	29.6 − 30.7	27.8 − 27.9	2.7	1.10	1.17	0.71	24.20
20110422_043824	60.0	19.6 − 28.6	13.9 − 23.2	26.6 − 27.1	27.0 − 27.5	−0.9	0.74	0.76	0.94	29.25
20110422_043924	28.0	5.0 − 30.0	14.7 − 26.3	26.1 − 30.0	26.6 − 27.4	2.4	0.41	0.51	1.13	40.01
20110529_101236	56.0	5.0 − 30.0	17.3 − 20.0	16.9 − 28.4	27.5 − 27.7	0.5	0.37	0.49	1.01	37.38
20110607_062044	60.0	8.7 − 10.3	20.9 − 30.0	27.8 − 28.0	26.5 − 26.5	0.9	0.63	0.96	NA	20.11
20110607_062144	48.0	8.2 − 9.2	25.8 − 28.2	28.3 − 28.5	26.8 − 26.8	1.1	0.70	1.03	NA	19.84
20110730_020652	36.0	5.0 − 11.6	17.4 − 27.7	27.5 − 28.3	26.8 − 27.0	0.4	0.36	0.50	NA	11.09
20110730_020732	24.0	20.4 − 29.0	19.4 − 22.3	28.2 − 28.3	28.4 − 28.5	−0.7	1.00	1.32	0.84	30.54
20110803_033428	52.0	19.3 − 22.4	17.0 − 18.1	27.2 − 27.4	28.0 − 28.2	−0.9	0.74	1.28	0.86	34.57
20110803_043016	44.0	5.0 − 13.6	18.0 − 27.0	27.2 − 27.8	26.9 − 27.0	0.3	0.27	0.50	NA	9.28
20110809_080028	60.0	15.0 − 25.6	17.8 − 21.7	27.2 − 27.8	27.6 − 27.8	−0.2	0.41	1.01	1.10	42.21

Date_time	δt	E_c(coronal)	E_c(photo)	Log($\mathcal{E}_t$) coronal	Log($\mathcal{E}_t$) photo	Log($\mathcal{E}_{diff}$)	χ^2 coronal	χ^2 photo	$R(Fe)$	$R_f(Fe)$
20110906_013736	60.0	5.0−21.4	5.0−21.1	27.4−30.8	27.5−30.9	2.9	1.53	1.80	0.62	22.44
20110906_013836	40.0	5.0−6.4	5.0−6.1	30.1−30.8	30.6−31.1	2.8	1.32	1.60	0.73	30.70
20110906_221556	60.0	20.9−22.6	19.7−20.3	27.5−27.6	27.8−27.8	−1.0	0.88	1.09	0.87	37.28
20110908_153616	36.0	6.2−10.4	5.0−30.0	27.9−28.8	25.8−25.9	1.2	0.95	1.13	NA	30.86
20110908_153656	60.0	5.0−30.0	5.0−30.0	26.6−26.8	26.6−26.7	−0.7	0.51	0.65	1.37	63.40
20110924_171944	60.0	21.3−25.3	18.3−22.4	27.6−27.7	27.6−28.0	−0.8	1.11	1.09	0.71	30.35
20110924_172044	60.0	5.0−5.7	5.0−5.3	31.6−31.9	31.8−31.9	3.1	1.10	1.44	0.60	26.81
20110924_191052	60.0	19.0−24.4	21.7−24.5	27.4−27.6	27.5−27.6	−0.5	0.96	1.16	0.97	49.26
20110924_203448	60.0	10.8−11.4	21.9−28.4	30.5−30.6	28.0−28.2	0.8	0.57	0.45	0.41	17.49
20110926_050544	40.0	5.0−5.5	5.0−6.1	29.5−29.8	29.1−29.6	2.3	2.26	2.20	NA	5.67
20111002_004144	60.0	16.1−24.8	18.5−23.9	26.9−27.3	27.1−27.2	−0.3	0.91	1.15	1.07	54.35
20111105_030920	60.0	17.7−20.0	17.9−19.3	27.4−27.7	27.5−27.7	−0.6	0.41	0.93	1.24	47.97
20111226_021836	60.0	5.0−30.0	5.0−30.0	25.8−26.0	26.1−26.7	−0.4	0.36	0.53	1.45	70.60
20111226_201544	60.0	18.7−27.8	18.8−24.3	27.1−27.3	27.4−27.5	−0.2	1.19	1.50	1.05	41.18
20111231_161908	60.0	5.0−7.0	16.8−23.0	28.4−28.8	26.8−27.0	1.6	1.65	1.88	NA	13.39
20111231_162008	28.0	8.0−10.2	5.0−30.0	28.0−28.4	25.7−25.9	1.2	1.32	1.71	NA	25.74
20121113_054512	36.0	5.8−7.0	6.2−7.4	29.2−29.5	28.6−29.0	2.2	0.49	0.47	NA	9.34
20121113_054556	60.0	5.0−6.1	5.0−6.1	30.6−31.1	30.5−31.0	2.9	0.56	0.63	0.70	29.89
20121114_040052	60.0	5.0−11.0	5.0−30.0	27.2−28.1	26.3−27.2	1.0	0.10	0.10	NA	5.23
20121114_040152	40.0	5.9−6.1	16.5−22.5	29.2−29.2	27.0−27.1	2.1	1.20	1.21	NA	12.38
20121120_123808	32.0	5.7−6.0	6.1−8.8	29.6−29.7	28.1−29.0	2.3	1.03	0.82	NA	27.42
20121120_123844	60.0	5.0−6.0	5.0−6.1	30.8−31.2	30.4−30.9	2.8	0.54	0.67	0.74	28.72
20121121_064812	44.0	6.9−7.0	7.8−26.8	29.3−29.3	27.1−28.5	1.8	0.79	0.78	NA	10.81
20121121_064900	60.0	5.0−8.2	16.5−20.1	29.5−30.7	27.6−28.0	1.8	0.99	0.96	0.57	19.97
20121128_213200	60.0	5.0−6.3	17.0−18.2	30.8−31.4	28.2−28.3	2.9	0.32	0.51	0.72	29.01
20121128_213300	60.0	5.0−6.5	5.0−30.0	30.9−31.6	26.0−26.2	2.9	0.39	0.99	0.76	29.40
20130111_085804	52.0	5.0−7.0	19.4−24.0	28.5−29.0	26.9−27.2	1.3	2.15	2.76	NA	14.26
20130111_085900	60.0	5.0−30.0	13.9−17.5	25.3−28.2	27.6−27.8	0.4	2.41	2.36	0.75	25.57
20130113_004744	48.0	5.0−14.1	14.7−30.0	27.1−27.5	26.8−26.9	0.2	0.30	0.41	NA	5.21
20130113_004840	60.0	5.0−9.3	16.6−17.8	29.1−30.9	28.2−28.3	2.0	0.62	0.89	0.78	26.82
20130217_154704	60.0	5.0−7.1	16.5−19.1	29.7−30.7	27.5−27.7	2.8	0.70	0.94	0.88	33.21

Table 1. Fitting results. Values (columns) for each time interval (row) are: interval date and time; derived limits for E_c using coronal and photospheric abundances; derived limits for $\mathcal{E}_t$ (total electron energy) for coronal and photospheric abundances; minimum (best-fit) values of *reduced* χ^2 using coronal and photospheric abundances; difference between $\mathcal{E}_t$ values for the derived E_c (coronal) and $E_c = 15$ keV; $R(Fe)$, the ratio of the count rate in the ∼6.7 keV Fe line complex to the peak of the count rate in the 10–20 keV range; and $R_f(Fe)$, the ratio of the fitted photon flux in the Fe line complex to the photon flux in the 10–20 keV range. For $R(Fe)$, "NA" means that there was no separate peak in the count spectrum, due to the fact that the thin attenuator was out.

Date_time	$Log(EM_{16})$ (cm^{-3})	$Log(N_{16})$ (cm^{-3})	$Log(V_{16})$ (cm^3)	$\tau_{Fe\text{XXV}}$ (s)	τ_{HEAT} (s)	$R_f(Fe,2)/R_f(Fe,1)$
20110213_173136,173236	47.4	10.4	26.5	5.	49.	1.13
20110215_014712,014812	47.4	10.3	26.8	7.	44.	0.90
20110216_142304,142404	47.7	10.5	26.7	4.	71.	1.24
20110228_124644,124744	47.4	10.3	26.8	6.	64.	1.20
20110307_194720,194820	47.0	9.9	27.3	18.	137.	0.97
20110307_214644,214744	47.3	10.4	26.6	6.	41.	1.17
20110309_231820,231920	48.1	10.4	27.3	5.	70.	0.89
20110314_194952,195108	48.6	11.0	26.6	1.	37.	1.12
20110422_043824,043924	47.5	10.5	26.5	4.	83.	1.37
20110607_062044,062144	45.9	9.3	27.3	64.	171.	0.99
20110730_020652,020732	47.9	10.5	26.9	4.	30.	2.75
20110906_013736,013836	47.4	9.9	27.5	15.	106.	1.37
20110908_153616,153656	47.2	10.2	26.7	8.	31.	2.05
20110924_171944,172044	47.6	10.5	26.5	4.	94.	0.88
20111231_161908,162008	46.1	9.8	26.5	20.	180.	1.92
20121113_054512,054556	47.0	9.9	27.2	17.	33.	3.20
20121114_040052,040152	45.5	9.2	27.1	79.	32.	2.37
20121120_123808,123844	47.3	10.1	27.2	11.	30.	1.05
20121121_064812,064900	46.9	9.8	27.3	21.	37.	1.85
20121128_213200,213300	48.1	10.9	26.4	2.	105.	1.01
20130111_085804,085900	46.9	9.9	27.1	16.	44.	1.79
20130113_004744,004840	47.6	10.2	27.1	8.	30.	5.15

Table 2. Results for evaluating ionization equilibrium for flares where two consecutive time intervals could be fit, using volume estimates from *RHESSI* images. For each flare (row), values (columns) are: EM_{16}, the total emission measure for plasma with $T > 16$ MK ($Log(T) > 7.2$), integrated from the DEM; N_{16}, the plasma density; V_{16}, the volume estimated from *RHESSI* images; $\tau_{Fe\text{XXV}}$, the time scale for ionization equilibrium of Fe XXV; τ_{HEAT}, the heating time scale, and the ratio of $R_f(Fe)$, Fe line to continuum flux ratios, for the second interval to the first interval.